Non-local self-energies in metals and itinerant magnets: A focus on Fe and Ni

Lorenzo Sponza, Paolo Pisanti, Alena Vishina, Dimitar Pashov, Cedric Weber, and Mark van Schilfgaarde
King's College London, London WC2R 2LS, UK

Julien Vidal
EDF and R&D, Department EFESE, 6 Quai Watier, 78401 Chatou, France

Gabriel Kotliar
Rutgers University, New Brunswick, NJ, USA
(Dated: January 25, 2022)

We present a new state-of-the-art theoretical approach to model correlated magnetic transition metal systems, by merging a form of self-consistent GW (QSGW) and dynamical mean field theory (DMFT). Recent high resolution ARPES and Haas-van Alphen data of two typical transition metal systems (Fe and Ni) are used as benchmark of the methodology. (i) Properties of Fe are very well described by QSGW alone, owing to its nonlocal character. Agreement with experimental data is excellent provided that final-state scattering is taken into account. (ii) Due to the presence of strong local spin fluctuations, QSGW alone is not able to provide a consistent description of the Ni ARPES data. To include spin fluctuations we develop a novel form of QSGW+DMFT where DMFT modifies the self-energy in the spin channel only. We also present a heuristic method to include spin fluctuations in QSGW by introducing an auxiliary effective magnetic field. Remarkable agreement is obtained with experiments by using our new methodology.

PACS numbers: 71.15.Mb,71.18.+y

High-resolution spectroscopy is limited in transition metals, in part because it is difficult to make sufficiently high quality samples. Fe is one element of which high quality films (with low dislocation densities) have been grown, and high-resolution angle-resolved photoemission spectroscopy (ARPES) performed [1]. Measurements were carried out at reasonably high energy (139 eV) where the penetration is deep enough that results are not affected by the surface, final states are free-electron like, and unwanted curvature of the electron's path on exiting the sample is smaller and better controlled. This experiment provides a good reference to test the validity of different approximations of the electronic structure.

There are also not many calculations of spectral functions in these materials. Fe has been studied in the local-density approximation (LDA) [2] and with corrections through Dynamical-Mean Field Theory (DMFT) [3]. It is not surprising that the LDA does not track the ARPES experiment well [4], but it has been found that LDA+DMFT also fails to properly account for ARPES data [3]. The GW approximation [5] is widely applied to many kinds of insulators, but how well it describes $3d$ transition metals is much less established.

Through quasiparticle self-consistency (QSGW) one determines the noninteracting Green's function G_0 which is minimally distant from the true Green's function G [6, 7]. Within QSGW many kinds of materials properties are in excellent agreement with experiment. These include quasiparticle band structures, Dresselhaus coefficients [8], electric field gradients [9], transmission probability [10], spin waves [11], and the dielectric response of many materials.

Another key property of QSGW is that, at self-consistency, the poles of $G_0(\mathbf{k},\omega)$ coincide with the peaks in $G(\mathbf{k},\omega)$. This means that there is no many-body "mass renormalization" of the noninteracting Hamiltonian, which allows for a direct association of QSGW energy bands $E(\mathbf{k})$ with peaks in the spectral function $A(\mathbf{k},\omega)$. Thus, QSGW provides an optimum framework to test the range of validity, and the limitations to the GW approximation.

In this work, we compare QSGW results [12] to various experimental data in elemental $3d$ materials in the Fermi liquid (FL) regime, with a heavy focus on Fe because of the high quality of ARPES [1] and de Haas-van Alphen (dHvA) [13, 14] data available. We will show that the QSGW and ARPES spectral function agree to within experimental resolution, with the proviso that the final state scattering is properly accounted in interpreting the experimental data. By contrast, discrepancies appear in Ni – a classical itinerant ferromagnet. This can be attributed to the lack of spin fluctuations in GW diagrams. To account for them in an *ab initio* manner we rely on a novel QSGW+DMFT implementation and we compare the results with a model correction.

Fe in the Fermi liquid regime

Fig. 1 compares the calculated QSGW band structure of Fe to peaks in ARPES spectra of Ref. [1], along with some inverse photoemission data [15]. While agreement appears to be very good, there are some discrepancies, particularly along the Γ-H line. This line is redrawn

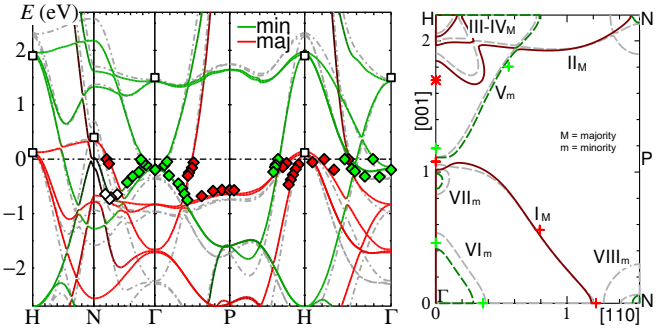

FIG. 1: (color online) Left: QSGW band structure of Fe (solid lines), LDA (dashed), ARPES spectra 1 (diamonds) and inverse photoemission spectra 15 (squares). Right: Fermi surface. Symbols denote FS crossings reported in Ref. 1. Red and green depict majority and minority d character, respectively.

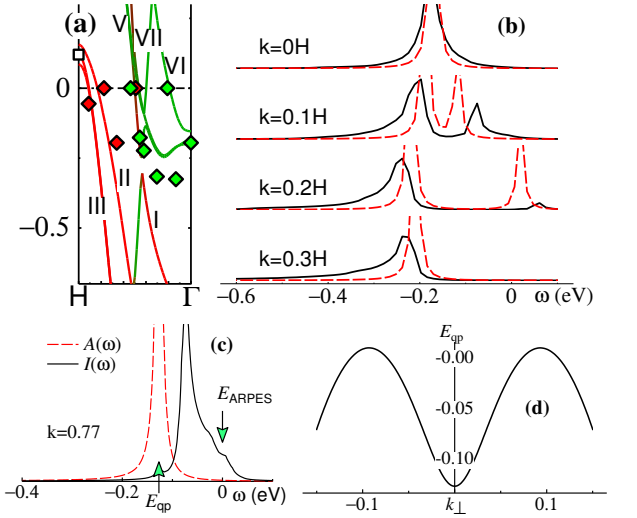

Band	Γ-H		Γ-N		Γ-P†	
	QSGW	ARPES	QSGW	ARPES	QSGW	ARPES
I	2.2	1.1	1.6	1.2	3.7	2.4‡
II	0.7	0.7				
V†	1.1	1.1			4.1	2.3‡
VI	0.8	0.7	1.2	0.8	1.3	0.9

†Along Γ-H, the two V bands are averaged. For the V band, the "Γ-P" column designates the H-P line. ‡Estimated from Figs. 10 and 13 in Ref.[1].

FIG. 2: (**a**): The Γ-H line of Fig. 1 in high resolution. Labels correspond to traditional assignments of Fermi surface pockets [1, 13]. (**b**): Dashed line is QSGW spectral function $A(k,\omega)$ for various points on Γ-H line, with k=0 and k=1 denoting Γ and H. Solid line is $A(\omega)$ modified according to Eq. (1). (**c**): the analog of (b) at k=0.77×H where the II$_M$ band crosses E_F. E_{QP} indicates the QSGW QP level, and E_{ARPES} the experimental ARPES peak at 0.77H. (**d**): dispersion in the QSGW II$_M$ band on a line $\mathbf{k}_\perp$ + [0,0,0.77H] normal to the film surface. Table compares Fermi velocities $\hbar v_F$ to ARPES measurements [1] (eV-Å).

on a finer scale in Fig. 2, to highlight the discrepancies. As noted earlier, the QSGW band structure reflects the peaks of $A(\mathbf{k},\omega)$ with no renormalizations from the ω- or $\mathbf{k}$- dependence of Σ.

In the FL regime, ARPES spectra $I(\mathbf{k},\omega)$ are generally thought to be a fairly direct measure of $A(\mathbf{k},\omega)$. But the two are not identical even in the FL regime, independently of the precision of the experimental setup. Assuming a one-step model [16] for the photoemission process (initial and final state coupled through Fermi's Golden rule [16, 17]) $I(\mathbf{k},\omega)$ can be written as

$$I(\mathbf{k},\omega) \propto \int dk_\perp |T_{fs}|^2 |M_{fi}(\mathbf{k}_\perp)|^2 A_f(\mathbf{k}_\perp) A(\mathbf{k},\omega), \quad (1)$$

$$\text{where } A_f(\mathbf{k}_\perp) = \frac{\Delta k_\perp/2\pi}{(\Delta k_\perp/2)^2 + (k_\perp - k_\perp^0)^2}$$

is the spectral function of the final state, broadened by scattering of the photoelectron as it approaches the surface [18]. T_{fs} is the final-state surface transmission amplitude and M_{fi} the photoexcitation matrix element (taken to be constant and $\mathbf{k}$-independent [19]). Thus the final state is considered to be a damped Bloch wave, taking the form of a Lorentzian distribution centred in $k_\perp^0$ and broadened by $\Delta\mathbf{k}_\perp$ [18], while the initial state is an undamped Bloch function with an energy broadening ΔE, obtained through the QSGW spectral function. This approximation is reasonable since in the FL regime $A(\mathbf{k},\omega)$ is sharply peaked around the QP level. $\Delta\mathbf{k}_\perp$ is directly related to the inverse of the electron mean free path. For photon energy in the range 100-130 eV, $\Delta\mathbf{k}_\perp \approx 0.2$ Å^{-1} [20, 21].

The final-state scattering broadens $I(\omega)$; but it also can shift the peak $\bar{\omega}$ in $I(\omega)$. The most significant discrepancy between ARPES and QSGW is found in the V$_m$ band, Fig. 2(a) between k=0 and 0.4×H. Fig. 2(b) shows $A(\mathbf{k},\omega)$ calculated by QSGW, and the corresponding $I(\mathbf{k},\omega)$ calculated from Eq. (1). Estimating the peak shift change from $\delta\bar{\omega} = \int d\omega\, \omega I / \int d\omega I - \int d\omega\, \omega A / \int d\omega A$, we find $\delta\bar{\omega}$<0.01 eV at Γ, increasing to $\delta\bar{\omega}\approx$0.06 eV for k between 0.1H and 0.3H. $\delta\bar{\omega}$=0.06 eV tallies closely with the discrepancy between the V$_m$ band and the measured ARPES peak for 0.1H<k<0.3H. There is also a significant discrepancy in the II$_M$ band near k=0.77×H. Where it crosses E_F, the QSGW bands deviate from the ARPES peak by nearly 0.15 eV. But ARPES simulated by Eq. (1) is much closer to experiment (Fig. 2(c)). This is understood from Fig. 2(d), which plots the QSGW dispersion along a line $\Delta\mathbf{k}_\perp$ normal to the film surface, passing through [0,0,0.77H]. A measurement that includes contributions from this line biases the ARPES peak in the direction of E_F since E$_{qp}$ is minimum at $k_\perp$=0. Thus we attribute most of the discrepancy in the Fermi surface crossing (red star in 1(b)) to an artifact of final-state scattering.

In order to pin down the errors in QSGW more precisely , we turn to de Haas-van Alphen (dHvA) measurements. Extremal areas of the FS cross sections can be extracted to high precision from frequencies observed in dHvA and magnetoresistance experiments. Areas nor-

TABLE I: de Haas-van Alphen measurements of extremal areas A on the [110] and [111] Fermi surfaces, in Å^{-2}. ΔE_F is an estimate of the error in the QP level (eV), as described in the text. Bottom panel: cyclotron mass, $m^*/m=(\hbar^2/2\pi m)\,\partial A/\partial E$.

FS	dHvA [110]			dHvA [111]		
pocket	QSGW	expt[13]	ΔE_F	QSGW	expt[13]	ΔE_F
I	3.355	3.3336	0.01	3.63	3.5342	0.04
II				3.694		
III	0.2138	0.3190	0.05	0.1627	0.2579	0.06
IV	0.0897	0.1175	0.04	0.0846	0.1089	0.02
VI	0.3176	0.5559	-0.13	0.2799	0.4986	-0.14
VII	0.0148	0.0405	0.04			
	m^*/m [110]			m^*/m [111]		
	QSGW	LDA	expt[23]	QSGW	LDA	expt[23]
I	2.5	2.0	2.6			
V				-1.7	-1.2	-1.7
VI				2.0	1.5	2.8

mal to [110] and [111] are given in Table I, along with areas calculated by QSGW. Fig.1 shows the QSGW Fermi surface, which closely resembles the one inferred by Lonzarich (version B) [22]. There is some difficulty (and ambiguity) in resolving the small VIII$_{\rm m}$ pocket at N because its tiny area is sensitive to computational details. Discrepancies in the extremal areas are not very meaningful: it is more sensible to determine the change ΔE_F in Fermi level needed to make the QSGW area agree with dHvA measurements. This amounts to the average error in the QSGW QP levels, assuming that the bands shift rigidly.

This assumption breaks down for the VI band because of strong electron-phonon renormalization, discussed below. Ref. 1 also extracts velocities $\hbar v_F$ at the Fermi surface from the k-dependence of ARPES peaks near E_F (see Table in Fig.2). Agreement is generally very good, except for a rather large discrepancy in the I band velocities. We analyse this discrepancy when discussing the cyclotron mass. Some limited cyclotron data for effective masses are also available [23]. These are expected to be more reliable than ARPES data. It is seen that agreement is excellent (Table I, bottom panel) except for the small VI pocket. We get a better comparison by accounting for the electron-phonon coupling with a simple model [24]. From the model, v_F is renormalized by a factor $1+\lambda=1.6$, which reasonably accounts for discrepancy between the QSGW and the cyclotron mass in pocket VI. The other pockets are much larger (Fig 1(b)), making v_F much larger on average, and the renormalization smaller. The cyclotron data enables us to assess the systematic difference in the QSGW and ARPES v_F for band I (Table in Fig. 2). The three points in the table serve as a reasonable estimate for the average velocity of the entire pocket, which cyclotron data measures. The fact that QSGW agrees well with cyclotron data strongly suggests the QSGW predictions at the individual points are more reliable than the ARPES data.

Ni: an archetypical itinerant magnet

Less detailed information is available for other elemental transition metals. We have extracted some experimental bandwidths, and also the exchange splitting ΔE_x in the magnetic elements. Fig. 3(a) shows that both seem to be very well described by QSGW, except that ΔE_x deviates strongly from experiment in Ni. QSGW significantly improves not only on the LSDA, but also on fully self-consistent GW [25] because of loss of spectral weight in fully self-consistent G that is avoided in QSGW [6].

Fig. 4 compares the QSGW band structure of Ni to ARPES data [26]. Agreement is excellent in the minority channel, but ΔE_x is uniformly too large on the symmetry lines shown. Also the band near -1 eV at L (consisting of s character there) is traditionally assumed to be a continuation of the d band denoted as white and green diamonds; but the calculations show that at it is a continuation of Ni s band. The corresponding LSDA band (light dotted lines) crosses L at $E_F-0.44$ eV; also the d bands are much wider.

ΔE_x is about twice too large in both QSGW and the LSDA, and for that reason spin wave frequencies are also too large [27]. Neither the LDA nor GW include spin fluctuations, which reduce the average moment and thus ΔE_x. Spin fluctuations $\langle M^2\rangle$ are important generally in itinerant magnets, and one important property they have is to reduce the average magnetic moment $\langle M\rangle$ [28, 29]. Fig. 3(b) shows this trend quite clearly: systems such as Fe, Co, and NiO are very well described by QSGW, but M is always overestimated in itinerant magnets such as FeAl, Ni$_3$Al, and Fe based superconductors such as BaFe$_2$As$_2$. Ni is also itinerant to some degree (unlike Fe, its average moment probably disappears as $T\to T_c$), and its moment should be overestimated. This is found to be the case for QSGW, as Fig. 3(b) shows.

Local spin fluctuations are well captured by localised non perturbative approaches, such as DMFT, and we can

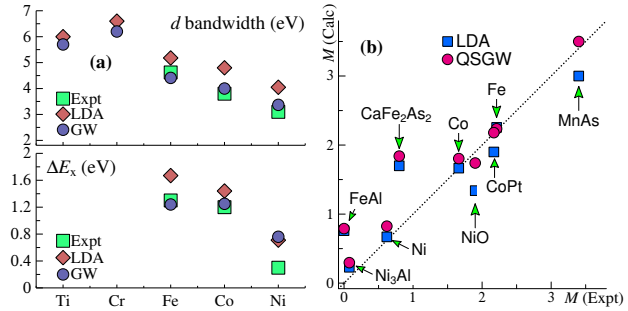

FIG. 3: (a): d bandwidth (top panel) and exchange splitting ΔE_x (bottom panel) in the 3d elemental metals. (b): Magnetic moment of several compounds

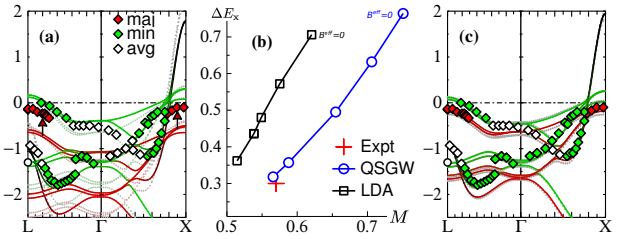

	LDA	QSGW	QSGW+$B^{\rm eff}$	QSGW+DMFT	Exp.
M	0.62	0.75	0.57	0.52	0.57
ΔE_x	0.71	0.77	0.32	0.25	0.31

FIG. 4: (color online) Band structure of Ni in QSGW (a) and QSGW+DMFT (c) with ARPES data [26] (the circle at -1.3 eV was taken from Ref. [30]). (b): ΔE_x at L as a function of M, obtained by adding an external magnetic field to the QSGW or LDA potential. In panel (a) the light dotted lines show LDA energy bands. Red arrows highlight the discrepancy in the exchange splitting ΔE_x at near L and X. In panel (c) the light dotted lines show bands (almost indistinguishable from the QSGW+DMFT band structure) generated by QSGW+$B^{\rm eff}$, with $B^{\rm eff}$ corresponding to the first circle in panel (b). Table: Magnetic moment M (Bohr) and exchange splitting ΔE_x@L (eV) at different levels of the theory compared to experiment.

reasonably expect that the addition of spin-flip diagrams to QSGW via, e.g. DMFT, would be sufficient to incorporate these effects. To verify this, we first assume that the predominant effect of spin fluctuations will result in an additional contribution to the static QSGW potential. This will be the case if the quasiparticle picture is a reasonable description of Ni, even if QSGW alone does not contain enough physics to yield an optimum quasiparticle approximation.

We first model spin fluctuations by carrying out the QSGW self-consistent cycle in the presence of a magnetic field $B^{\rm eff}$, and tuning $B^{\rm eff}$ to reduce M. Our key finding is that when $B^{\rm eff}$ is tuned to make M agree with experiment, ΔE_x does also, reproducing ARPES spectra to high precision in the FL regime. Both the QSGW and LSDA overestimate M for itinerant systems, but the latter also *underestimates* it in local-moment systems (Fig. 3(b)). In the LSDA treatment of Ni, these effects cancel and render the moment fortuitously good. When spin fluctuations are folded in through $B^{\rm eff}$, the LSDA moment becomes too small.

For an adequate *ab initio* foundation we note that QSGW does an excellent job at handling the important diagrams (especially screening) in a parameter-free way, apart from the spin-flip contributions. On the other hand these latter are largely local, and they are well taken into account with DMFT. A G_0W_0+DMFT study of ferromagnetic Ni can be found in [31, 32]. Here we adopt a novel implementation of QSGW+DMFT. The DMFT part relies on the Continuous Time Quantum Monte Carlo solver implemented by K. Haule [33]; correspondingly the projection and embedding schemes implemented in our QSGW suite follow the prescriptions of reference [33] which are outlined in the supplemental material [24].

We carry out a DMFT calculation on the Ni d orbitals with the intent of extracting a static correction to the QSGW calculation. The bath is computed with a spin-averaged exchange correlation potential from QSGW Σ_1 to which we add the static part of the spin-flip correction Σ_2 obtained from a complete DMFT loop [24]. The two potentials, Σ_1 with no spin part, and Σ_2 with no charge part, do not overlap so that Σ_2 may be added to Σ_1 without double counting.

The results, shown in Fig. 4(c) and summarised in the corresponding Table, report a quenching of both ΔE_x and M with respect to the QSGW calculation. A similar trend was found in [3] (LDA+DMFT) and [31] (G_0W_0+DMFT) in comparison with the LDA benchmark. It is worth stressing that our results not only agree very well with the experimental values, but they are also almost indistinguishable from the semi-empirical QSGW+$B^{\rm eff}$ ones (cf. Fig. 4(c)).

Conclusions

To summarize, we have performed detailed QSGW calculations of the electronic band structure of several $3d$ metallic compounds to assess the reliability of this theory in the Fermi liquid regime.

Focusing our analysis mostly on Fe and Ni, for which very high quality ARPES measurement (plus dHvA and cyclotron data for Fe) are available, we conclude that QSGW provides very accurate description of the band structure around E_F. We also made a brief survey of other $3d$ magnetic transition metals, finding correspondingly good agreement, except in the itinerant case of Ni where spin fluctuations become important.

– ***Fe:*** Through de Haas-van Alphen and cyclotron measurements we established that QSGW QP levels at E_F have an error of $\sim$0.05 eV, and effective masses are well described. Comparable precision is found below E_F by comparing to ARPES data, provided final state scattering is taken into account. The QSGW d bandwidth falls in close agreement with ARPES, and is approximately 0.75 times that of the LDA (Fig. 1).

If Σ is k-averaged to simulate a local self-energy, the QSGW band structure changes significantly and resembles the LDA. Thus non-locality in the self-energy is important in transition metals, and its absence explains why LDA+DMFT does not yield good agreement with ARPES [3].

– ***Ni:*** QSGW d bandwidths, the t_{2g}–e_g splitting, the s–d alignment, are all in excellent agreement with experiment, while $\langle M\rangle$ and ΔE_x are too large. Fortuitous error

cancellation partly conceals failings of the LSDA, which yield good $\langle M\rangle$ but overestimates ΔE_x.

To account for spin fluctuations, we established that the addition of a constant to QSGW calculations $B^{\rm eff}$ eliminates discrepancies in both $\langle M\rangle$ and ΔE_x. To account for spin fluctuations in an *ab initio* framework, we constructed a novel QSGW+DMFT implementation with the self-energy in the charge channel carried by GW and the spin channel by DMFT, thus avoiding ambiguities in double-counting. The magnetic moment and band structure from a quasiparticlized Hamiltonian was essentially identical in the the two cases showing that (at least for Ni) spin fluctuations are very well approximated by a static, constant field. Beside the fundamental relevance of this result, this conclusion is of particular interest also for technical reasons, especially when calculations on large magnetic systems are concerned.

This work was supported by the Simons Many-Electron Collaboration, and EPSRC grant EP/M011631/1. The authors gratefully acknowledge computer resources from the Gauss Centre for Supercomputing e.V. (www.gauss-centre.eu). We also acknowledge the Partnership for Advanced Computing in Europe (PRACE) for awarding us access to the following resources: Curie FN and TN based in France at the Très Grand Centre de Calcul (TGCC), and SuperMUC, based in Germany at Leibniz Supercomputing Centre.

SUPPLEMENTAL MATERIAL

Survey on the QSGW theory

Quasiparticle self-consistency is a construction that determines the noninteracting Green's function G_0 that is minimally distant from the true Green's function G. A measure of distance, or metric is necessary; a good choice [6] results in an effective static potential:

$$\bar{\Sigma}^{\rm xc} = \frac{1}{2}\sum_{ij} |\psi_i\rangle \left\{ {\rm Re}[\Sigma(\varepsilon_i)] + {\rm Re}[\Sigma(\varepsilon_j)]_{ij} \right\} \langle\psi_j|. \quad (2)$$

$\Sigma_{ij}(\omega)$ is the self-energy in the basis of single-particle eigenstates $|\psi_i\rangle$, which becomes iG_0W in the GW approximation. Starting from a trial G_0, e.g. the LDA, $\bar{\Sigma}^{\rm xc}$ is determined through GW, which determines a new G_0. The cycle is repeated until self-consistency.

Recently Ismail-Beigi showed that Eq. 2 also minimizes the gradient of the Klein functional, $|\delta F|^2$, where F is evaluated in the subspace of all possible static $\bar{\Sigma}^{\rm xc}$ [7].

Another key property of Eq. 2 is that, at self-consistency, the poles of $G_0(\mathbf{k},\omega)$ coincide with the peaks in $G(\mathbf{k},\omega)$. Therefore the band structure generated by $V^{\rm xc}$ coincides with the peaks of the specral function $A(\mathbf{k},\omega)$. This is significant, because it means there is no many-body "mass renormalization" of the noninteracting hamiltonian. In other words, the attribution of mass renormalization to correlation effects, a concept widely used in the literature [4], is ill-defined: it depends on an arbitrary reference, e.g. the LDA. The absence of mass renormalization is a very useful property: we can directly associate QSGW energy bands $E(\mathbf{k})$ with peaks in the spectral function $A(\mathbf{k},\omega)$.

Electron-phonon renormalization of effective masses

In the region VI of the Fermi surface, the agreement between the computed $m*/m$ and the experiment is not as good as for the other regions (see Table I in main text). To improve the agreement, we accounted for the electron-phonon renormalization in a simple way.

According to a Thomas-Fermi model of screening [34], the elecron-phonon interaction renormalizes v_F by a factor $1+\lambda$. Band VI is roughly spherical, enabling us to evaluate λ analytically:

$$\lambda = \frac{e^2}{\hbar v_F}\left[\frac{1}{2}\ln\frac{k_{TF}^2}{k_{TF}^2+k_F^2} + \frac{k_F}{k_{TF}}\arctan\frac{k_F}{k_{TF}}\right] \quad (3)$$

Estimating k_F=1.71 Å^{-1} from the Fe electron density, this leads to a renormalization factor of 1.6.

Remembering that $v_F \propto 1/m*$, we can compare this factor with the ratio $m^*_{\rm QSGW}/m^*_{\rm exp} = 1.4$, which is close to the estimated contribution from the electron-phonon interaction.

Computational details

*QS*GW

For the high resolution needed here, computational conditions had to be carefully controlled.

In both QSGW calculations of Fe and Ni, a k mesh of 12×12×12 divisions was found to be sufficient for calculating Σ. The one-body part was evaluated on a 24×24×24 mesh.

Fe $3p$ and $4d$ states were included through local orbitals: omitting these and treating $3p$ as core levels [6] can shift QP levels by as much as 0.1 eV in the FL regime. Other parameters [6], such as broadening the pole in G in constructing Σ=iGW, the basis of eigenfunction products, and the energy cutoff for the off-diagonal parts of Σ, were also carefully monitored. When set to tight tolerances QP levels near E_F were stable to a resolution of 0.05 eV. QP levels are calculated including spin-orbit coupling (SOC), though it is omitted in the calculation of Σ. The effect of SOC on Σ was found to make small changes to $\bar{\Sigma}^{\rm xc}$.

Similar parameters were used in the QSGW calculation for Ni.

*QS*GW+*DMFT*

Concerning the QSGW+DMFT calculation on Ni, we projected the lattice problem on the Ni d orbitals following the prescription of Haule [35]. We compute higher level diagrams locally using the hybridization expansion version of the numerically exact continuous time QMC method [33, 36].

In order to single out the correlated subspace, a procedure of projection/embedding which was originally introduced in [35] in the LAPW basis of the Wien2k package, is developed in the Full-Potential Linear Muffin-Tin Orbitals (FP-LMTO) basis [37]. This projector maps the full space Green's function $G_{ij\mathbf{k}}$ (with band and k-point label $\{ij\mathbf{k}\}$) to the local Green's function $G^{\rm loc}_{LL'}$ defined only on the correlated subspace. The compact index $L := \{\tau, R, \sigma, \ell, m\}$, collects information on the atom type τ, site R, spin coordinate σ, and angular momentum components ℓ and m. The projection operation can be cast in the following form:

$$G^{\rm loc}_{LL'} = \sum_{\mathbf{k},ij} U^L_{i\mathbf{k}}\, G_{ij\mathbf{k}}\, U^{L'\dagger}_{j\mathbf{k}} \quad \text{with} \quad U^L_{i\mathbf{k}} \propto \sum_u \mathcal{A}^L_{i\mathbf{k}} \Phi^u_{R\ell}\ ,$$

where the coefficients $\mathcal{A}^L_{i\mathbf{k}}$ account for localization inside the sphere, while $\Phi^u_{R\ell}$ gives an estimate of correlations relative to the specific orbital component ℓ. More specifically $\mathcal{A}^L_{i\mathbf{k}}$ are linear combinations of spherical harmonics $Y_{\ell m}$ and the QSGW quasiparticle eigenfunctions in the FP-LMTO basis. The terms $\Phi^u_{R\ell}$ are radial integral of the kind $\langle \varphi^u_{R\ell} | \varphi_{R\ell} \rangle$ where the index u in $\varphi^u_{R\ell}$ indicates the possibility of selecting the radial solution $\varphi_{R\ell}$ of the Schrödinger equation inside the MTO, its energy derivative $\dot{\varphi}_{R\ell}$, and its local orbitals contributions $\varphi^z_{R\ell}$ [6]. By means of these definitions we ensure that the localized orbitals are centred on the correlated atom corresponding to the muffin-tin site R.

The transformation matrices U have been orthonormalised in such a way that $\sum_{i\mathbf{k}} U^L_{i\mathbf{k}} U^{L'\dagger}_{i\mathbf{k}} = \delta_{LL'}$.

The local Green's function is defined on a grid of Matsubara frequencies $i\omega_n = i\pi(2n+1)/\beta$ and it is employed to calculate the hybridization function of the system, which feeds the CTQMC impurity solver. The result of the impurity solver is the local impurity self-energy $\Sigma^{\rm loc}_{LL'}(i\omega)$ also defined on the Matsubara axis. In order to update the full Green's function $G_{ij\mathbf{k}}$ with this local self-energy, so to iterate the DMFT loop to self-consistency, an embedding procedure is needed. Because of the specific properties of the transformation U, the embedding procedure $\Sigma^{\rm loc}_{ij\mathbf{k}}(i\omega) = \sum_{LL'} U^{L\dagger}_{i\mathbf{k}} \Sigma^{\rm loc}_{LL'}(i\omega) U^{L'}_{j\mathbf{k}}$ can be operated by means of the same matrices, even though this is not a general requirement of the theory [35].

In our application to Ni, we extrapolated the static components of $\Sigma^{\rm loc}_{LL'}(i\omega)$, we embedded it into the lattice problem and we kept only its symmetrized real part

$$\bar{\Sigma}^{\rm loc}_{ij\mathbf{k}} = \frac{1}{2}\left[{\rm Re}\left(\Sigma^{\rm loc}_{ij\mathbf{k}}(i\omega=0)\right) + {\rm Re}\left(\Sigma^{\rm loc}_{ji\mathbf{k}}(i\omega=0)\right)\right]. \quad (4)$$

This is done for the spin-up and spin-down channels separately. We finally retained only the spin-flip component $\Sigma_2 = \bar{\Sigma}^{\rm loc} - (\bar{\Sigma}^{\rm loc}_\uparrow + \bar{\Sigma}^{\rm loc}_\downarrow)/2$ and we added it to the charge component $\Sigma_1 = (\bar{\Sigma}^{\rm xc}_\uparrow + \bar{\Sigma}^{\rm xc}_\downarrow)/2$ computed at QSGW level, as explained in the main text. This procedure allowed us to prevent counting twice the magnetic contributions to the self-energy.

The projectors used for the Ni $3d$ are constructed from 5 bands below E_F and 3 bands above E_F, which correspond to a window of $\sim\pm10$ eV. By choosing a wide energy window, U becomes nearly static [38]. The corresponding on-site Coulomb parameters were chosen to be U=10 eV and J=0.7 eV, close to the values calculated by constrained RPA [38]. The Matsubara frequency grid is defined over 2000 points with an inverse temperature $\beta = 50$ eV^{-1}.

The charge double-counting contribution has been included by means of the standard formula

$$E_{dc} = U(n-1/2) - J(n/2-1/2)$$

where n is the nominal occupancy of the $3d$ shell. Instead, the magnetic double-counting has been avoided by computing the charge contribution to the self-energy in only within QSGW and extracting the spin contribution from the DMFT calculation, as better explained in the main text.

Nine iterations of the DMFT loop (each composed by projection + CTQMC + embedding) have been necessary to converge the static limit of the impurity self-energy. At each iteration, around 10^{10} random moves have been done to solve the impurity problem.

[1] J. Schäfer, M. Hoinkis, E. Rotenberg, P. Blaha, and R. Claessen, Phys. Rev. B **72**, 155115 (2005)
[2] J. Callaway and C. S. Wang, Phys. Rev. B **16**, 2095 (1977)
[3] J. Sánchez-Barriga, J. Fink, V. Boni, I. Di Marco, J. Braun, J. Minár, A. Varykhalov, O. Rader, V. Bellini, F. Manghi, H. Ebert, M. I. Katsnelson, A. I. Lichtenstein, O. Eriksson, W. Eberhardt and H. A. Dürr, Phys. Rev. Lett. **103**, 267203 (2009)
[4] A. L. Walter, J. D. Riley, and O. Rader, New J. Phys. **12**, 013007 (2010)
[5] L. Hedin, J. Phys.: Condens. Matter **11**, R489 (1999)
[6] T. Kotani, M. van Schilfgaarde, and S. V. Faleev, Phys. Rev. B **76**, 165106 (2007)
[7] S. Ismail-Beigi, arXiv:1406.0772 (2014)
[8] A. N. Chantis, M. van Schilfgaarde , and T. Kotani, Phys. Rev. Lett **96**, 086405 (2006)
[9] N. E. Christensen, A. Svane, R. Laskowski, B. Palanivel, P. Modak, A. N. Chantis, M. van Schilfgaarde, and T. Kotani, Phys. Rev. B **81**, 045203 (2010)

[10] S. V. Faleev, O. N. Mryasov, and M. van Schilfgaarde, Phys. Rev. B **85**, 174433 (2012)

[11] T. Kotani and M. van Schilfgaarde, J. Phys.: Condens. Matter **20**, 295214 (2008)

[12] Our implentation (bitbucket.org/lmto) was adapted from the original ecalj code at github.com/tkotani/ecalj.

[13] D. R. Baraff, Phys. Rev. B **8**, 3439 (1973)

[14] A. Gold, J. Low Temp. Phys. **16**, 3 (1974)

[15] A. Santoni and F. J. Himpsel, Phys. Rev. B **43**, 1305 (1991)

[16] J. Pendry, Surface Science **57**, 679 (1976)

[17] R. Matzdorf, Surface Science Reports **30**, 153 (1998)

[18] V. N. Strocov, J. Elec. Spect. and Rel. Phenomena **130**, 65 (2003)

[19] V. N. Strocov, R. Claessen, G. Nicolay, S. Hüfner, A. Kimura, A. Harasawa, S. Shin, A. Kakizaki, P. Nilsson, H. Starnberg, *et al.*, Phys. Rev. Lett **81**, 4943 (1998)

[20] P. J. Feibelman and D. Eastman, Phys. Rev. B **10**, 4932 (1974)

[21] S. Tanuma, C. J. Powell, and D. R. Penn, Surface and Interface Analysis **21**, 165 (1994)

[22] G. G. Lonzarich, in *Electrons at the Fermi surface*, edited by M. Springford (Cambridge University Press, 1980)

[23] A. V. Gold, L. Hodges, P. T. Panousis, and D. R. Stone, Int. J. Magn **2**, 375 (1971)

[24] For further details on the electron-phonon coupling model and the QSGW+DMFT implementation, see Supplemental Material at the end of the main text.

[25] K. D. Belashchenko, V. P. Antropov, and N. E. Zein, Phys. Rev. B **73**, 073105 (2006)

[26] F. J. Himpsel, J. A. Knapp, and D. E. Eastman, Phys. Rev. B **19**, 2919 (1979)

[27] K. Karlsson and F. Aryasetiawan, Phys. Rev. B **62**, 3006 (2000)

[28] I. Mazin, D. Singh, and A. Aguyao, arXiv:cond-mat/0401563

[29] M. Shimizu, Rep. Prog. Phys. **44**, 329 (1981)

[30] W. Eberhardt and E. W. Plummer, Phys. Rev. B **21**, 3245 (1980)

[31] S. Biermann, F. Aryasetiawan and A. Georges, Phys. Rev. Lett. **90**, 086402 (2003)

[32] The main accomplishment of work [31] was actually to reproduce at the GW+DMFT level the satellite structure at ∼-6 eV, already captured by Lichtenstein and coworkers [3] in a previous LDA+DMFT calculation. The investigation of this spectral feature is currently under study with our implementation.

[33] K. Haule, Phys. Rev. B **75**, 155113 (2007)

[34] N. W. Ashcroft and D. Mermin, *Solid State Physics* (Brooks/Cole, 1976)

[35] K. Haule, C. H. Yee, and K. Kim, Phys. Rev. B **81**, 195107 (2010)

[36] P. Werner, A. Comanac, L. de Medici, M. Troyer, and A. J. Millis, Phys. Rev. Lett. **97**, 076405 (2006)

[37] M. Methfessel, M. van Schilfgaarde and R. A. Casali, *Electronic Structure and Physical Properties of Solids: The Uses of the LMTO method, Lecture Notes in Physics*, vol. 535 (Springer-Verlag, Berlin, 2000)

[38] S. Choi, A. Kutepov, K. Haule, M. van Schilfgaarde, and G. Kotliar, arXiv:1504.07569 (2015)